Solar RRL
www.solar-rrl.com

Understanding Ion-Related Performance Losses in Perovskite-Based Solar Cells by Capacitance Measurements and Simulation

Christoph Messmer, Jonathan Parion, Cristian V. Meza, Santhosh Ramesh, Martin Bivour, Minasadat Heydarian, Jonas Schön, Hariharsudan S. Radhakrishnan, Martin C. Schubert, and Stefan W. Glunz*

Understanding the behavior of mobile ions in perovskite-based solar cells (PSCs) is crucial for improving their performance and stability, which belong to the key hurdles in advancing this technology toward commercialization. This study explores the role of mobile ions in PSCs using the comprehensive technology computer-aided design model which is extended to simulate the frequency-dependent capacitance (*C–f*) of PSCs. It is compared with equivalent circuit approaches showcasing the validity and advantages of full device modeling. By combining the simulation of full measurement procedures with *C–f* and *J–V* measurements on experimental test structures, the observed *C–f* characteristics can be quantitatively related to performance losses in scan-time-dependent *J–V* curves, both originating from ion diffusion. With this combined analysis, insights can be provided on the physical origin and interpretation of the different *C–f* plateaus caused by the displacement of ions. Finally, the *C–f* characteristics of PSCs under illumination and the impact of band alignment and recombination at the perovskite interface are investigated. Experimental PSCs with and without electron-transport layer passivation are fabricated, showing a good agreement between the simulated and measured *C–f* and pointing toward a lower surface recombination for the passivated PSC. This study shows how drift-diffusion modeling helps to characterize and interpret capacitance-based data.

1. Introduction

Understanding and mitigating the migration of mobile ions in perovskite-based (tandem) solar cells (PSCs) remain one of the greatest challenges toward their commercialization, affecting both device performance and stability.[1–7] Characterization of ion-related losses is therefore of great importance for highly efficient and reliable PSCs. Capacitance-based methods are widely used for emerging solar cell technologies like PSCs to assess internal device parameters like built-in potentials, doping densities, mobilities, and many more.[8,9] However, the validity and applicability of these methods for PSC are not straightforward and information obtained from capacitance-based methods for PSC needs to be revised as pointed out, e.g., by Ravishankar et al.[10] While previous studies contributed to the understanding of the complex interplay of capacitances within PSCs even without considering ionic movement,[10] a recent publication on transient capacitance

C. Messmer, J. Schön, S. W. Glunz
INATECH
Chair for Photovoltaic Energy Conversion
University of Freiburg
Emmy-Noether-Str. 2, 79110 Freiburg, Germany
E-mail: christoph.messmer@ise.fraunhofer.de,
christoph.messmer@inatech.uni-freiburg.de

C. Messmer, M. Bivour, M. Heydarian, J. Schön, M. C. Schubert, S. W. Glunz
Division Photovoltaics
Fraunhofer Institute for Solar Energy Systems ISE
Heidenhofstr. 2, 79110 Freiburg, Germany

The ORCID identification number(s) for the author(s) of this article can be found under https://doi.org/10.1002/solr.202400630.

DOI: 10.1002/solr.202400630

J. Parion, C. V. Meza, S. Ramesh, H. S. Radhakrishnan
imec Division IMOMEC
Thorpark 8320, 3600 Genk, Belgium

J. Parion, C. V. Meza, S. Ramesh, H. S. Radhakrishnan
EnergyVille
Thorpark 8320, 3600 Genk, Belgium

J. Parion
Hasselt University
Wetenschapspark 1, 3590 Diepenbeek, Belgium

C. V. Meza
Department of Electrical Engineering
KU Leuven
Kasteelpark Arenberg 10, 3001 Leuven, Belgium

measurements in PSCs[11] has shown further experimental evidence, suggesting that multiple ion species are involved. However, besides few publications,[7] priorly used simulation models lack the consideration of more than one type of ion species, as well as the relation to more commonly assessed measurements like reverse and forward scans of current–voltage curves (*J*–*V*).

Within the scope of this work, a comprehensive and experimentally validated optoelectrical simulation model[5] for PSCs in Sentaurus technology computer-aided design (TCAD)[12] was extended to simulate frequency-dependent capacitance–voltage (*C*–*f*) characteristics, with the ability to consider different types of mobile ions. Our study focuses on PSCs with bandgaps of 1.83 and 1.53 eV intended for use as top and middle cell in a perovskite/perovskite/silicon triple-junction solar cell, respectively. However, the simulation model is generally applicable to any kind of perovskite-based device, including perovskite/silicon tandem and triple-junction solar cells.[5,13] In a first section, we introduce the TCAD model and the modeling approach for small-signal AC analysis, followed by a model validation against previous modeling approaches like equivalent circuit (EC) models, including showcases of the impact of geometrical capacitances and the influence of doped contacts and Schottky barriers. In the following section, the impact of mobile ions is elaborated in a general simulation study, followed by experimental validation with perovskite single-junction solar cells that were fabricated and measured at IMEC determining their current–voltage (*J*–*V*) characteristics, as well as the capacitance–frequency (*C*–*f*) behavior. The *C*–*f* and *J*–*V* measurements demonstrate good agreement with the simulation model. The study could correlate the ionic properties derived from *C*–*f* characterization to the observed scan-time-dependent hysteresis of measured *J*–*V* curves, providing valuable insights into the behavior of mobile ions and their impact on PSC performance. By means of the simulation model, we provide insights on the physical origin and interpretation of the different *C*–*f* plateaus caused by the displacement of ions. In the last subsection, we investigate the *C*–*f* characteristics of PSCs under illumination and the impact of band alignment and recombination at the perovskite interface. For this, experimental PSCs with and without electron-transport layer (ETL) passivation were fabricated at Fraunhofer ISE and measured at IMEC, showing a good agreement between the simulated and measured *C*–*f*. The objective of this research is to enhance the comprehension of capacitance-based methods applied to PSCs and to learn what information can (and cannot) be extracted from capacitance measurements. We aim to validate and improve the interpretability and reliability of capacitance-based characterization methods, contributing to effective design strategies for enhancing PSC performance.

2. TCAD Model for Small-Signal AC Analysis

2.1. Modeling Approach

We approach this topic by means of a comprehensive optoelectrical simulation model in Sentaurus TCAD[12] which we developed in several previous publications and is capable to describe the detailed physics of perovskite-based single-junction and tandem solar cells based on coupled Poisson and drift-diffusion equations, both for electron/holes and for several types of mobile ions (anions and cations). A detailed description of the simulation model and experimental validation was published by Messmer et al.[5] The model was extended within the scope of this publication to be capable for small-signal AC analysis which computes the frequency-dependent admittance matrix *Y* of the specified electrical system, i.e., the PSC. For a given excitation frequency *f*, it describes the equivalent small-signal model by[12]

$$\delta I = Y \cdot \delta V \tag{1}$$

where δV and δI are the vectors of (complex-valued) voltage and current excitations at the electrodes, respectively. The admittance matrix can be represented as

$$Y = A + i2\pi f \cdot C \tag{2}$$

with the real-valued conductance matrix *A*, the frequency *f*, and the capacitance matrix *C*.

This work focuses on the capacitance response, i.e., the imaginary part of the admittance matrix *Y*, but the model can also be used for other types of impedance analysis, e.g., by Nyquist plots.

2.2. Model Validation and Comparison to EC Models

We compared our drift-diffusion model (referred to as DD or TCAD model in the following) to approaches in previous publications for consistency checks and evaluation of the differences. **Figure 1**a shows an EC (or multilayer) model of a perovskite single-junction solar cell as used, e.g., by Ravishankar et al.[10] The EC model consists of a series resistance R_S, an ETL, perovskite layer (Pero), followed by a hole-transport layer (HTL). Each layer is represented by a resistor–capacitor (*RC*) circuit. The capacitor accounts for the geometrical capacitance C_L per area *A* of each layer *L*, given by

$$C_L/A = \varepsilon_0 \varepsilon_r / d_L \tag{3}$$

where ε_r is the relative permittivity and d_L is the thickness of layer *L*. The resistor R_L of each layer *L* is connected in parallel to the capacitor and accounts for the layer conductivity. Each *RC* circuit causes a frequency dependence of the capacitance with characteristic frequency:

$$f_L = (2\pi \cdot R_L C_L)^{-1} \tag{4}$$

$$= (2\pi \cdot (\rho_L \cdot d_L)(C_L/A))^{-1} \tag{5}$$

where ρ_L is the resistivity of layer *L*. In our TCAD model, we can calculate the resistivity ρ_L in dependence of the depth *z* via the parallel resistivity of electrons and holes according to

$$\rho_L(z) = (\sigma_e(z) + \sigma_h(z))^{-1} \tag{6}$$

where $\sigma_{e,h} = q \cdot \mu_{e,h} \cdot n_{e,h}$ is the electron (hole) conductivity, respectively. For each layer *L*, the local resistivity can be integrated to obtain the total contribution of the layers' series resistance:

$$R_L \cdot A = \rho_{tot} \cdot d_L = \int_0^{d_L} \rho_L(z) dz \tag{7}$$

which can be used in Equation (5) to calculate f_L and is furthermore used as input value for comparison with the EC model.

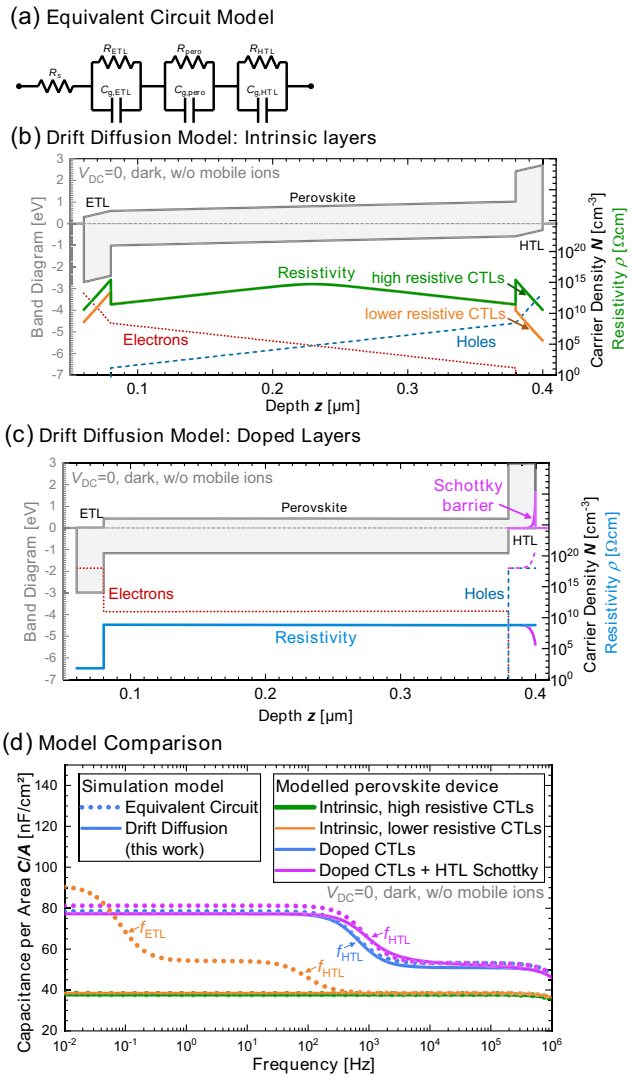

Figure 1. a) Schematic overview of a typical EC model. b) Band diagram (without applied DC bias in the dark) of an all-intrinsic perovskite single junction with Schottky contacts derived from the DD model in Sentaurus TCAD; the right axis refers to the electron/hole densities and local resistivity. c) Band diagram from the DD model of an perovskite single junction with doped CTLs and band offsets chosen to get constant resistivity within each layer. d) Frequency-dependent capacitance per area C/A for four different scenarios comparing the EC model of (a) dotted lines, with the DD model of (b) and (c) solid lines (this work).

In the following, we will present four scenarios which show the conformity of our TCAD model with previous work (i.e., the EC model) and afterward we elaborate on why the models differ:

The first scenario can be seen in Figure 1b, where the band diagram of a simple PSC is shown as obtained from the TCAD model for the case of intrinsic (i.e., undoped) layers. It consists of an undoped ETL with very low mobility of 10^{-5} cm^2 Vs^{-1}, next to a Schottky contact with a work function of 4.2 eV and aligned to the conduction band of the intrinsic perovskite. The hole contact consists of an intrinsic HTL with the same low mobility of 10^{-5} cm^2 Vs^{-1}, next to a Schottky contact with a work function of 5.2 eV and aligned to the valence band of the perovskite. The detailed simulation parameters can be found in Table S1, Supporting Information. The right axis of Figure 1b shows the electron and hole densities as red dotted and blue dashed lines, respectively, as well as the corresponding resistivity $\rho_L(z)$ as solid green line according to Equation (6) (note the different units for the resistivity on the right axis). One can see that the simulation parameters have been chosen in a way to obtain "symmetric" electron/hole densities and resistivities; however, the intrinsic layers lead to an inhomogeneous resistivity distribution throughout each layer. Furthermore, Figure 1b shows a second example for lower resistive CTLs by choosing higher charge-carrier mobilities of 10^{-3} and 1 cm^2 Vs^{-1} for the ETL and HTL, respectively. While the band diagram and electron/hole densities stay unchanged, the resulting resistivity in the CTLs is decreased by two and five orders of magnitude, respectively, as can be seen by the solid orange line in Figure 1b.

A third scenario can be seen in Figure 1c which shows the band diagram of a PSC from the DD model with doped layers (and with ohmic contacts instead of Schottky contacts). The electron (hole) density within the ETL (HTL) was chosen in such a way that the ETL (HTL) Fermi level is very close to the conduction (valence) band. Furthermore, the perovskite layer features a work function which is slightly shifted from mid-bandgap toward the conduction band (realized by very low n-doping). The conduction (valence) band offset at the ETL/perovskite (perovskite/HTL) interface was chosen in such a way that the vacuum Fermi levels of each layer are equal and therefore no built-in potential can be seen within the perovskite layer. All parameters have been chosen to achieve a homogeneous (i.e., constant) electron and hole density, and thus, resistivity within each layer, as can be seen by the red dotted, blue dashed, and solid blue line, respectively, which all refer to the right axis in Figure 1c. As a fourth scenario, we modeled a Schottky contact with a very high work function of 6 eV in contact with the HTL, which accumulates holes in the proximity of the HTL/Schottky interface leading to a lower resistivity, as shown by the highlighted lines in magenta on the right side of Figure 1c.

These four scenarios in Figure 1b,c are now used to elaborate on where the DD model is in agreement with the EC model and in which cases it would predict a different behavior of the total capacitance of the perovskite device. Figure 1d shows the simulated capacitances C (per area A) as a function of the small-signal AC frequency f at a DC voltage $V_{DC} = 0$ V for both the EC (dotted lines) and DD model (solid lines), whereby the colors are consistent with the colors used for the resistivity distributions of the four scenario in Figure 1b,c.

We first compare the first scenario of the perovskite device with "intrinsic layers, high resistive CTLs" in Figure 1b, green. As all three layers L are undoped and featuring low mobility, the overall resistivities are quite high (i.e., each $R_L \cdot A > 10^8\,\Omega\,\mathrm{cm}^2$); therefore, the characteristic frequencies are all quite low (i.e., each $f_L < 10^{-2}$ Hz). Both models yield the same baseline capacitance (shown in Figure 1d, green lines) which is the total geometrical capacitance $C_{g,tot}$ calculated as a series connection of the three single capacitance $C_{g,L}$ (according to Equation (3)):

$$\frac{1}{C_{g,tot}/A} = \frac{1}{\varepsilon_0\varepsilon_{r,ETL}/d_{ETL}} + \frac{1}{\varepsilon_0\varepsilon_{r,Pero}/d_{Pero}} + \frac{1}{\varepsilon_0\varepsilon_{r,HTL}/d_{HTL}} \quad (8)$$

Therefore, the simulation results are equal as long as the characteristic frequencies of the intrinsic layers are lower than the regarded frequency regime. However, when regarding the second scenario with "intrinsic layers, lower resistive CTLs" as shown in Figure 1d in orange, the EC model predicts three capacitance plateaus (orange dotted lines) due to the two characteristic frequencies f_L of the ETL and HTL at 0.13 and 130 Hz, respectively, while the DD model predicts the same baseline capacitance as before (here, the $\varepsilon_{r,Pero}$ has been slightly increased from 30 to 31 to make the two cases distinguishable). This is a serious discrepancy inside an experimentally relevant frequency range which has to be discussed: One main difference between the EC model and the DD model is the assumption that the depth-dependent resistivity $\rho_L(z)$ inside an intrinsic layer can be represented by a single ohmic (therefore homogenous) resistor R_L according to Equation (7). As can be seen in Figure 1b, the resistivity is distributed highly inhomogeneous in all three intrinsic layers (note the logarithmic scale of the right axis). The two CTLs feature the highest resistive contribution at the proximity to the respective perovskite interface while ≈94% of the total resistivity of the (intrinsic) perovskite layer lie inside the middle third of the perovskite bulk, while the two outer thirds of the perovskite bulk contribute only ≈3%, respectively. However, for "doped" perovskite layers, this asymmetry in resistivity distribution within the perovskite layer would be lower. Note that for multilayer models like in Ravishankar et al.[10] the perovskite bulk resistance is also a recombination resistance, where they assume shielding of the electric field in the perovskite by mobile ions. This assumption leads to a more homogenous resistivity distribution within the perovskite absorber which could result in a better overlap between the DD model and the EC model for the case of undoped layers.

The third example as shown in Figure 1c with "doped CTLs" showcases a device where the resistivity is homogenously distributed within each layer. In Figure 1d, it can be seen by the blue lines that the EC model (dotted blue) and DD model (solid blue) show a good agreement under this assumption of homogenous resistivity. The characteristic frequency of the HTL, which can be calculated according to Equation (4) to be $f_{HTL} = 966$ Hz, is consistent with both modeling approaches. We also tested the influence of an (almost) infinite dielectric permittivity of the perovskite absorber (see Figure S1a, Supporting Information) and the influence of a very high ion concentration (see Figure S1b, Supporting Information), both resulting in a complete screening of the electrical field within the perovskite bulk leading to a constant resistivity distribution. However, the built-in field is then present within the ETL/HTL layer. This results in a very inhomogeneous resistivity distribution within these layers that leads to differences between the EC and DD model.

As a last example, the influence of a potential Schottky barrier is showcased in Figure 1c. The resistivity $\rho_{HTL}(z)$ is lowered in proximity to the Schottky contact (shown in magenta), which leads to a lower R_{HTL} as input for the EC model. Figure 1d shows that both the EC (dotted magenta) and the DD model (solid magenta) predict a higher characteristic frequency of the HTL $f_{HTL} = 1390$ Hz which is consistent with the lowered resistivity according to Equation (4). However, the slightly increased inhomogeneity of the layer's resistivity increases the discrepancy between the models; while Sentaurus predicts the same low-frequency capacitance plateau as in the third case (solid blue vs solid magenta), the EC model predicts a higher low-frequency capacitance plateau (dotted blue vs dotted magenta) due to the overall lower resistor R_{HTL} which lead to a higher "bypass" of the $C_{g,HTL}$ within the series connection of capacitances.

In conclusion, we have seen that the DD model is consistent with previous EC modeling. However, discrepancies with equivalent circuit models were shown for cases where the depth dependence of one or several layers is highly inhomogeneous. In these cases, we would recommend the detailed device modeling over equivalent circuit approaches.

3. Results

In this section, mobile ions are included in the TCAD model and their influence on the frequency-dependent capacitance is assessed. In the first subsection, the general impact is discussed in terms of a simulation study. In the second subsection, the TCAD model is validated by experimental data showing the link between capacitance and *J*–*V* hysteresis. The detailed simulation parameters used for this section can be found in Table S2, Supporting Information. In the third subsection, an in-depth analysis of the origin of the capacitance plateaus originating from ionic movement is carried out. The last subsection extends the study to illuminated capacitance–frequency analysis where recombination properties play an important role.

3.1. Ion-Induced Capacitances in Perovskite Absorbers: Simulation Study

Figure 2 shows the simulated capacitance *C* per area *A* of a perovskite single junction as function of the applied frequency *f* of the

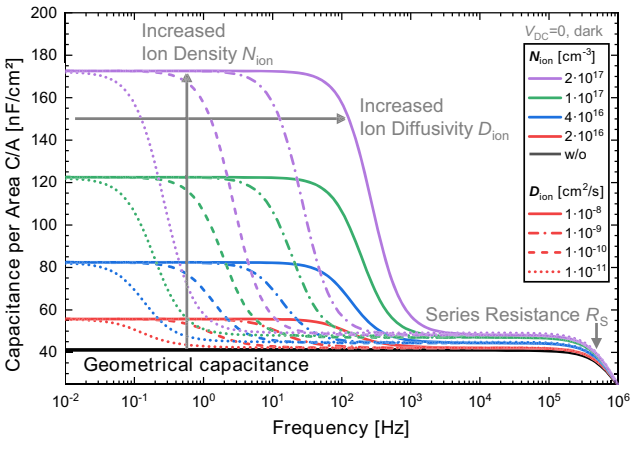

Figure 2. Simulated capacitance *C* per area *A* of a perovskite single junction as function of the frequency for varied anion densities (N_{ion}, different colors) and anion diffusivities at 25 °C (D_{ion}, different line styles), as well as without any ions in the model ("geometrical capacitance," black line), all for $V_{DC} = 0$ and without illumination. One can see the influence of increased ion density and diffusivity as shown by the arrows as well as the impact of the cell series resistance R_S in the high-frequency region.

AC signal for a fixed DC voltage of 0 V and for varied anion properties (while the cations are assumed to be homogenous distributed and immobile). First, the black line shows the behavior of the capacitance C in the absence of mobile ions in the perovskite absorber. One can see a constant capacitance plateau of around $C/A = 41\,\mathrm{nF\,cm^{-2}}$ for frequencies below 10^5 Hz which corresponds to the geometrical capacitance $C_{g,Pero}$ of the perovskite absorber according to Equation (3) with $\varepsilon_{r,Pero} = 19.5$ and $d_{Pero} = 420\,\mathrm{nm}$. Since the ETL and HTL were assumed to be low resistive ($\rho < 10^{-4}\,\Omega\,\mathrm{cm^2}$), the geometrical capacitances of the ETL and HTL do not contribute to the effective C_g in this special case which is in line with the EC model for low resistances R_{ETL}/R_{HTL}.[10] The high-frequency drop above 100 kHz can be attributed to the ohmic series resistance R_S of the device and was adapted to $3\,\Omega\,\mathrm{cm^2}$ according to measurements of similar perovskite single junctions that were fabricated.

In a second step, anions are included in the model featuring variations of the anion density N_{ion} (Figure 2, different colors) and anion diffusivity D_{ion} (different line styles), while cations with density N_{ion} are assumed to be immobile (which is a good assumption due to their commonly very low diffusivities, so that they would barely move at all during typical times of measurement, see ref. [5]) and homogeneously distributed (Note that the concrete distribution of cations has influence on the results, as it impacts the effective built-in potential and effective charge-carrier extraction. This will be discussed in Section 3.3. However, the assumption of a fixed and homogeneous cation distribution is still valid since the effective properties of the extraction layers and the effective built-in potential within the simulation were chosen according to the choice of cation distribution.) within the perovskite absorber. For N_{ion} smaller than $1 \times 10^{15}\,\mathrm{cm^{-3}}$, no difference can be observed with respect to the black line in Figure 2 (not shown). This is in line with the lower limit of resolution $N_{d,min}$ according to ref. [14] ranging between 1×10^{15} and $5 \times 10^{15}\,\mathrm{cm^{-3}}$ for a perovskite absorber thickness of $d = 420\,\mathrm{nm}$ and the dielectric permittivity of $\varepsilon_r = 19.5$. Starting in this range of N_{ion}, both a noticeable difference in C–f signal (with respect to the black line in Figure 2) and a significant J–V hysteresis in the simulated reverse and forward scan occur (as shown in the Supporting Information, see Figure S1, Supporting Information). For $N_{ion} >> N_{d,min}$, a capacitance plateau with increasing magnitude for increasing N_{ion} occurs. For an anion diffusivity of $D_{ion} = 10^{-8}\,\mathrm{cm^2\,s^{-1}}$ (solid lines), the characteristic frequency of the transition occurs in the range of $\approx 10^2$ to 10^3 Hz. For slower diffusivities, the plateau shifts to the left, i.e., to lower frequencies (shown by different line types). Each order of magnitude in higher diffusivity corresponds to an order of magnitude in lower frequency.

3.2. Relation of C–f Characteristics and J–V Hysteresis: Experimental Evidence

In a next step, we elaborate on the impact of ion migration on the capacitance–frequency characteristics and its relation to typically observed J–V hysteresis, based on both simulation and experimental devices. For experimental validation, a perovskite single-junction solar cell with an active area of 0.125 $\mathrm{cm^2}$ was fabricated at IMEC. **Figure 3**a shows the layer stack of the device. The 420 nm thick perovskite with bandgap of 1.53 eV was deposited via "hybrid route" on an indium tin oxide (ITO)-coated glass substrate with a 15 nm thick nickel oxide (NiO) layer acting as hole-transport material. The electron contact is featuring a 1 nm thick lithium fluoride (LiF) layer which acts as contact displacement layer[15] for the 40 nm thick C_{60}/BCP layer, serving as electron-transport material, followed by a full-area silver contact.

Figure 3b shows the measured capacitance per area C/A as function of the frequency f for the experimental perovskite test structure as blue dotted line, as well as the simulated data from the TCAD model for an ion density of $N_{anion} = 5.2 \times 10^{16}\,\mathrm{cm^{-3}}$ and an anion diffusivity of $D_{anion} = 6.0 \times 10^{-10}\,\mathrm{cm^2\,s^{-1}}$ (at 25 °C) shown as blue solid line. The cations were assumed to be immobile during the simulated measurement procedure. First of all, one can see a very good quantitative agreement of the simulation and experiment, with a slightly smoother transition between the two capacitance plateaus for the experiment with respect to simulated data which has been observed before when comparing experimental to modeled data.[16] This could be explained by device inhomogeneities which smoothen out the sharpness of this transition in the experiment, such as, e.g., laterally inhomogeneous perovskite thickness or other nonuniformities of the perovskite layer. Generally, it is important to understand which device properties and, thus, which simulation input parameters have an impact in the modeling of the frequency-dependent capacitance, and how ambiguous the choice of simulation parameters actually is. Starting with the intermediate frequency plateau C_{IF}/A in Figure 3b, we assumed for the simulation that the electron and hole densities in the respective C_{60} and NiO layer is high enough to ensure good extraction properties (despite their typically low charge-carrier mobilities[17]); therefore, they feature a low resistivity (i.e., each $R_L \cdot A < 10^{-3}\,\Omega\,\mathrm{cm^2}$). Under this assumption, the geometrical capacitances of both CTLs can be neglected and the intermediate capacitance plateau can be approximated by

$$C_{IF}/A \approx \varepsilon_0 \varepsilon_{r,Pero}/d_{Pero} \tag{9}$$

where $d_{Pero} = 420\,\mathrm{nm}$ is known from measurements. Therefore, in this case the relative permittivity of the perovskite absorber could be determined from the intermediate capacitance plateau to $\varepsilon_{r,Pero} = 19$. Note that the approximation of Equation (9) is not only valid when the resistances of the transport layers play a role, as it could be the case for low-mobility/low-doped CTLs which are well known in the literature.[17–19]

Furthermore, from the high-frequency transition in Figure 3b, typically the effective ohmic series resistance R_S can be extracted. Unfortunately, the high-frequency regime above 10^5 Hz was not measured for the very same sample. However, it could be measured for a follow-up batch, which is shown in Figure 3b as an inset (top right corner). The experimental capacitance C divided by the designated area A (transparent dots) is slightly higher than for the first batch which could be due to a slightly different dielectric constant $\varepsilon_{r,Pero}$ and/or uncertainties of the designated area of $A = 0.125\,\mathrm{cm^2}$ (The contact deposition that was done by evaporation through a mask might have some not well-defined edges that could increase the area to a higher value than intended.). The variation of the R_S in the simulation model is shown as solid lines from 0 (black) to $4\,\Omega\,\mathrm{cm^2}$ (yellow). When shifting the

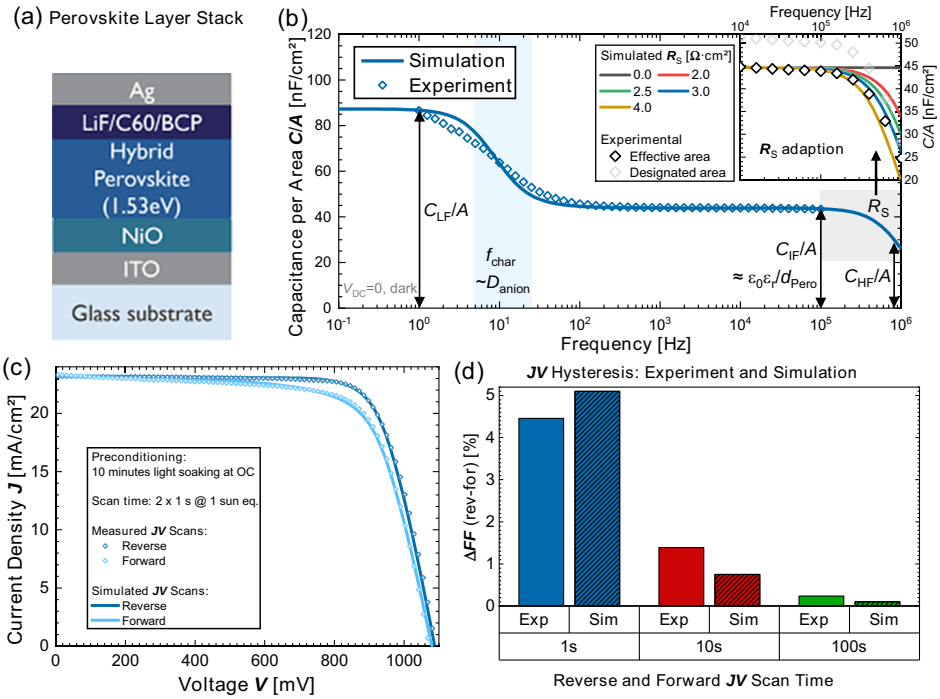

Figure 3. a) Layer stack of the investigated perovskite single junction as built in-house at IMEC. b) The measured frequency-dependent capacitance (blue diamonds) for $V_{DC} = 0$ V in the dark can be well replicated by the simulation model with an anion density of $N_{anion} = 5.2 \times 10^{16}$ cm^{-3} and an anion diffusivity of $D_{anion} = 6.0 \times 10^{-10}$ cm^2 s^{-1}, derived from the characteristic frequency f_{char} (blue shaded area), as well as the effective ohmic series resistance R_S from the high frequency regime (gray shaded area, see inset). c) The properties of the mobile ion as determined in (b) are directly linked to the *J*–*V* hysteresis of the measured (dotted) and simulated (solid) *J*–*V* reverse (dark blue) and forward (light blue) scans. d) Scan-time-dependent hysteresis can be replicated very well by the simulation (cross-hatched bars) compared to the experimental measurements.

experimental data to the plateau of the simulation at 10^4 Hz (black dots, "effective area"), the comparison of experiment and simulation gives an estimate for the experimental series resistance of $R_S \approx 3\,\Omega\,\text{cm}^2$ (blue line) which has been used as input for the simulation model both in Figure 3.

Finally, the low-frequency plateau C_{LF}/A in Figure 3b was assigned to originate from ion migration. Generally, the interpretation of the origin of capacitance steps has to be handled with care, as, principally, also characteristic frequencies of purely geometrical capacitances could occur in the respective experimentally accessible frequency range as showcased in Section 2.2, Figure 1d, by the blue solid line. However, there is some indication that the experimentally measured frequency dependence originates from mobile ions. First, the characteristic frequencies of the ETL and HTL can be estimated to be $f_{ETL,HTL} > 10^6$ Hz due to their low resistivity. Furthermore, the extracted ionic diffusivity $D_{anion} = 0.6 \times 10^{-9}$ cm^2 s^{-1} is in line with prior publications, where the anion diffusivity was determined from scan-time-dependent *J*–*V* measurements to lie in the order of magnitude of $D_{anion} = 10^{-9}$ cm^2 s^{-1}.[5] Third, the scan-time-dependent *J*–*V* measurements match quite well using this diffusivity of ions.

Figure 3c shows the current density–voltage (*J*–*V*) curves of the experimental (dotted curves) and the simulated PSC (solid curves) using the same simulation parameter set as obtained from Figure 3b. Both the experimental and simulated cell have been preconditioned under 10 min of light soaking at open-circuit conditions, followed by a subsequent reverse scan (dark blue) and a forward scan (light blue). One can see that the observed *J*–*V* hysteresis can be very well described by the simulation model using the ionic properties as priorly determined from *C*–*V* measurements.

Figure 3d shows that also the scan-time characteristics of the *J*–*V* hysteresis,[5] represented by the difference in fill factor between reverse and forward *J*–*V* scan, can be replicated very well by the simulation (cross-hatched bars) compared to the experimental measurements for three different orders of magnitude in scan time variation, ranging from a *J*–*V* scan time of 1 s (blue bars, corresponding to *J*–*V* scan of Figure 3c), 10 s (red bars), and 100 s (green bars). The respective scan-time-dependent *J*–*V* curves can be found in Figure S3, Supporting Information.

While the relation of the characteristic frequency in the *C*–*f* curves to the ion diffusivity is obvious and seems to be relatively unambiguous (also indicated by the simulation study in Figure 2), the interpretation of the height of the low-frequency plateau C_{LF}/A has to be interpreted with great care. The simulation study of Figure 2 seems to suggest that the height of the low-frequency plateau C_{LF}/A could be directly linked to the ion density present in the absorber. However, the relation of C_{LF}/A to the ion density is not as straightforward as it is entangled with other device properties, especially the built-in electric field within the perovskite absorber, and therefore dependent on both charge-transport layers (CTLs) and the band alignment at the ETL/perovskite and perovskite/HTL interface (not shown here). Thus, the same amount of ion concentration could lead to

different heights of C_{LF}/A when the band offset between layers is altered in the simulation model. (An explanation for this will be given in the next subsection, where an in-depth analysis of the increased device capacitance caused by ionic displacement is showcased.)

Summing up this section, we see that the capacitance–frequency measurements and simulations can contribute to the analysis of device properties; however, the interpretation of capacitance plateaus and characteristic frequencies has to be handled with great care. It is stressed again that the low-frequency plateau C_{LF}/A in Figure 3b as a separate result does not allow to assess the ion concentration. Only with a comprehensive set of data, e.g., including (scan-time-dependent) J–V measurements and further characterization, an incremental interpretation of the internal device properties and correlation of ionic migration to performance losses of the J–V characteristics is sensible.

3.3. In-Depth Analysis of Ion-Induced C–f Plateaus

After comparing the simulation model to previous work in Section 2.2 and careful validation by means of the experimental data in Section 3.2, we would like to share insights obtained from the simulation model to contribute to the understanding of the ion-induced frequency dependence of the device capacitance of the PSC and give a quantitative interpretation of the device physics as well as where the additional capacitance is originating from.

Figure 4a shows the simulated band diagram in the dark without externally applied voltage as derived from Figure 3. It consists of an ETL with high electron density and a low conduction band offset toward the perovskite layer which effectively takes into account the contact displacement due to the 1 nm thick LiF layer (which is not explicitly modeled here). The HTL is modeled as a p-type NiO layer in direct contact with the n-type ITO electrode. The transport of majority charge-carriers is realized by efficient recombination of holes from the NiO side with electrons from the ITO side, which is modeled by Shockley-Read-Hall recombination at the ITO/NiO interface with a lifetime of 1 ps, which ensures that the transport at this interface is nonlimiting. The right axis refers to the electron (red), hole (blue), anion (green), and cation (magenta) densities across the device. This band diagram and the charge-carrier densities refer to the "initial state" right before the C–f analysis; therefore, all changes in carrier densities are understood as difference to Figure 4a.

Figure 4b then shows the change in carrier densities ΔN for electrons (red colors), holes (blue colors), and anions (green colors), while the cations have too low diffusivity to move during the regarded time scale (therefore not shown) (As the in-house AC tool of Sentaurus TCAD does not allow to assess band diagrams at specific intermediate points, we decided to additionally develop an own tool which approximates the sine wave by a linear voltage function and extracts the band diagrams and charge-carrier densities at the maximum voltage of the AC excitation signal, which has been chosen to be 100 mV in this case. The difference in densities shown in Figure 4b refers to the difference between the state of maximum AC excitation and no excitation. We also tested the influence of the AC excitation voltage (ranging from 10 to 100 mV), which influences the delta in

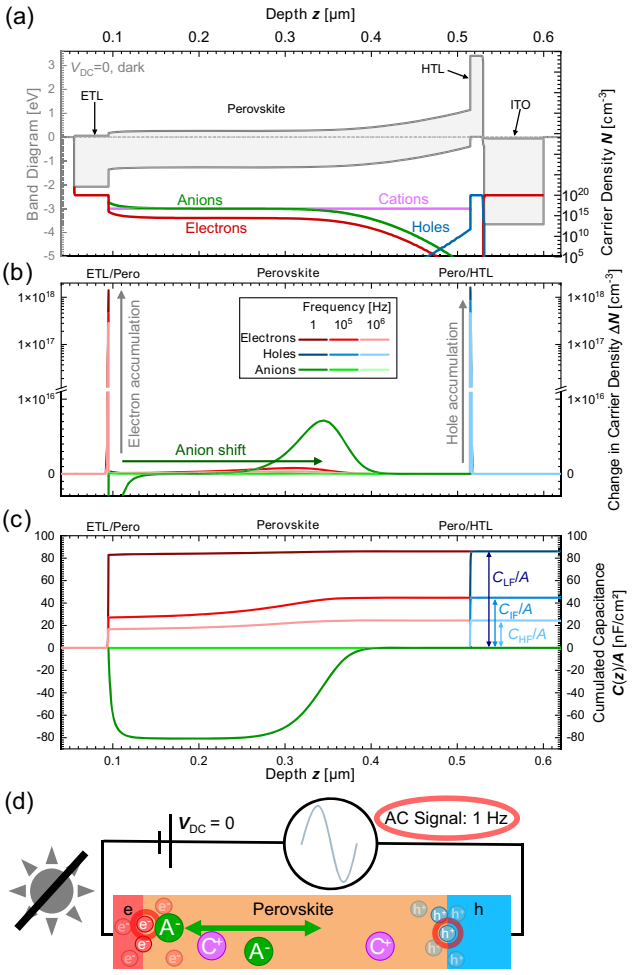

Figure 4. a) Band diagram (left axis) of the experimentally validated model of Figure 3 in the dark without applied voltage featuring an ETL/perovskite/HTL/ITO layer stack. The right axis shows the electron, hole, anion, and cation carrier densities, respectively. b) Change in carrier densities with respect to (a) for electrons (red), holes (blue), and anions (green), when a small AC signal is applied, shown for a high frequency (10^6 Hz, light colors), an intermediate frequency (10^5 Hz, normal colors), and a low frequency (1 Hz, dark colors); for the latter case the anion shift from the ETL interface toward the bulk is highlighted. c) The cumulated (i.e., integrated) charges per voltage (i.e., capacitance) according to Equation (10), showcasing the depth dependence of the device capacitance of Figure 3b. d) A schematic sketch of the low-frequency case.

charge-carrier densities in a linear behavior, while the capacitances as calculated and shown in Figure 4c are in accordance (with only minor deviations) with the capacitances from the sophisticated in-house Sentaurus AC tool, which was used everywhere else in this work, which shows that the linear approximation made for Figure 4 can be justified in this case.). The different shadings refer to the high-frequency case of 10^6 Hz (light colors), intermediate-frequency case of 10^5 Hz (normal colors), and low-frequency case of 1 Hz (dark colors), all three cases correspond to the respective arrows highlighted in Figure 3b.

Starting with the high-frequency case of 10^6 Hz (light colors), one could see a high electron accumulation in the proximity of

the ETL/perovskite interface (light red) with a peak of $\approx 3 \times 10^{17}\,\mathrm{cm}^{-3}$ (note the logarithmic scaling after the disruption of the y-axis), and a high hole accumulation in the proximity of the HTL/perovskite interface (light blue) with the similar peak height of $\approx 3 \times 10^{17}\,\mathrm{cm}^{-3}$. Note that these densities are dependent on the used AC excitation voltage, which has been chosen to be 100 mV in this case. Furthermore, a very low additionally accumulation of electrons can be seen in the perovskite bulk around $z = 0.3\,\mu\mathrm{m}$. This first case corresponds to an AC frequency that is in the transition regime of the ohmic series resistance R_S.

The second case with the frequency of 10^5 Hz corresponds to the case where the ohmic series resistance R_S is nonlimiting, but the characteristic frequency of the anions is too low (or, in other words, they are "too slow"). Figure 4b shows an additional electron accumulation in the proximity of the ETL/perovskite interface (normal red) with a peak of around $5 \times 10^{17}\,\mathrm{cm}^{-3}$ and an additional hole accumulation in the proximity of the HTL/perovskite interface (normal blue) with the similar peak height of $\approx 5 \times 10^{17}\,\mathrm{cm}^{-3}$. Furthermore, an additional accumulation of electrons can be seen in the perovskite bulk around $z = 0.3\,\mu\mathrm{m}$.

Finally, the third case with the frequency of 1 Hz (dark colors) corresponds to the case where anions can move. Figure 4b shows an anion displacement from the ETL/perovskite interface (i.e., $\Delta N_{\mathrm{anions}}$ is negative) represented by the dark green line toward the perovskite bulk (i.e., positive $\Delta N_{\mathrm{anions}}$) with a maximum $\Delta N_{\mathrm{anions}}$ around $z = 0.35\,\mu\mathrm{m}$. As the negatively charged anions "compete" with the negatively charged electrons, as a result, Figure 4b shows that the ionic displacement away from the interface results in another additional electron accumulation in the proximity of the ETL/perovskite interface (dark red) with a peak of around $1.5 \times 10^{18}\,\mathrm{cm}^{-3}$; the hole accumulation at the HTL/perovskite interface is increased analogously (dark blue).

Figure 4c finally shows the cumulated (i.e., integrated) capacitance per area in dependence of the device depth according to

$$C(z)/A = \frac{e}{\Delta V_{\mathrm{ac}}} \int_0^z \Delta N(z')\mathrm{d}z' \tag{10}$$

where e is the elementary charge, $\Delta N(z')$ is the change in carrier density at depth z' (according to Figure 3b), and ΔV_{ac} is the amplitude of the applied AC voltage. Figure 4c shows for the three capacitances C_{HF}, C_{IF}, and C_{LF} of Figure 3b (that are highlighted by the arrows, respectively), and how they are quantitatively distributed within the perovskite device. Starting with the high-frequency case, we can see in Figure 4c that the cumulated C_{HF}/A (shown by the arrow in light blue) amounts to $23\,\mathrm{nF\,cm}^{-2}$ for the total device (which is in line with the high-frequency case in Figure 3b), whereby the total hole capacitance of $23\,\mathrm{nF\,cm}^{-2}$ is located at the Pero/HTL interface (shown in light blue), and the electron capacitance is divided between ≈70% at the Pero/ETL interface ($\approx 16\,\mathrm{nF\,cm}^{-2}$) and ≈30% in the middle of the bulk ($\approx 7\,\mathrm{nF\,cm}^{-2}$). For the intermediate capacitance plateau (i.e., $f = 10^5$ Hz), Figure 4c shows a cumulated C_{IF}/A (shown by the arrow in normal blue) amounts to $44\,\mathrm{nF\,cm}^{-2}$ for the total device (which is in line with the intermediate-frequency case in Figure 3b), whereby the total hole capacitance of $44\,\mathrm{nF\,cm}^{-2}$ is located at the Pero/HTL interface (shown in normal blue), and the electron capacitance is again distributed within the device, with around 61% at the Pero/ETL interface ($\approx 27\,\mathrm{nF\,cm}^{-2}$) and a ≈39% in the middle of the bulk ($\approx 17\,\mathrm{nF\,cm}^{-2}$). For the low-frequency capacitance plateau (i.e., $f = 1$ Hz, Figure 3b), where anions could move, Figure 4c shows that C_{LF}/A (shown by the arrow in dark blue) amounts to $86\,\mathrm{nF\,cm}^{-2}$ for the total device (which is again in line with the low-frequency case in Figure 3b), whereby the total hole capacitance is again located at the Pero/HTL interface (shown in dark blue), and the electron capacitance is now mostly located at the Pero/ETL interface ($\approx 83\,\mathrm{nF\,cm}^{-2}$) and only a minor fraction in the perovskite bulk ($\approx 3\,\mathrm{nF\,cm}^{-2}$). Additionally, Equation (10) was also applied to the anions as shown in Figure 4c by the green curves. Only for the low-frequency case, anions could move, which is reflected by the dark green curve showing a negative slope in the local capacitance in the proximity of the ETL/perovskite interface (i.e., anions vanished there) and a positive slope of the local capacitance between $z = 0.3$ and 0.4 μm (i.e., anions accumulated there). The total integral is zero, as anion density is constant within the simulation model. Most interestingly, the minimum value of the anion capacity of $-81\,\mathrm{nF\,cm}^{-2}$ around $z = 0.2\,\mu\mathrm{m}$ quantifies the amount of anion charges which moved away from the ETL interface, namely, $Q/A = -5 \times 10^{10}\ \mathrm{e/cm}^2$, which is only about 2.3% of the total anion charges within the whole perovskite absorber ($N_{\mathrm{anions}} = 5.2 \times 10^{16}\,\mathrm{cm}^{-3}$; $d_{\mathrm{Pero}} = 420\,\mathrm{nm} \rightarrow Q_{\mathrm{anions}}/A = -2.2 \times 10^{12}\,\mathrm{e\,cm}^{-2}$). Therefore, to draw inferences from the low-frequency capacitance plateau C_{LF}/A in Figure 3b about ion concentrations within the perovskite is not (directly) possible. However, one can learn a lot from this capacitance plateau about the ability of the device to displace ions from interfaces which in the end is also entangled with the electric field of the perovskite absorber (thus built-in potential from the extraction layers). The latter could also be influenced by long-term migration of the relatively slow cations,[20] which effectively deteriorate the built-in potential and selectivity of the extraction layers. Generally, this also indicates that other closely related characterization methods such as the bias-assisted charge extraction method[21] should be interpreted with great care, as the amount of charges extracted in a low-frequency (i.e., larger timescale) regime does not coincide with the extract amount of ions within the perovskite absorber.

3.4. Frequency-Dependent Capacitance under Illumination

In this section, the capacitance response of illuminated PSCs was studied by means of the TCAD model, and experimental test structures were fabricated at Fraunhofer ISE and measured at IMEC.

3.4.1. Simulation Study

Figure 5a shows the simulated capacitance per area C/A as a function of the AC frequency at a DC voltage $V_{\mathrm{DC}} = 0\,\mathrm{V}$ under illumination of 1 sun equivalent (colored solid lines). The impact of varied ETL/perovskite interface properties is shown by the different colors: First, the solid blue line shows the TCAD simulation of the experimentally validated perovskite device (as shown in Figure 3) with a conduction band offset at the ETL/perovskite interface $\Delta E_{\mathrm{C}}^{\mathrm{ETL}}$ of 0.1 eV (which is in line with literature values

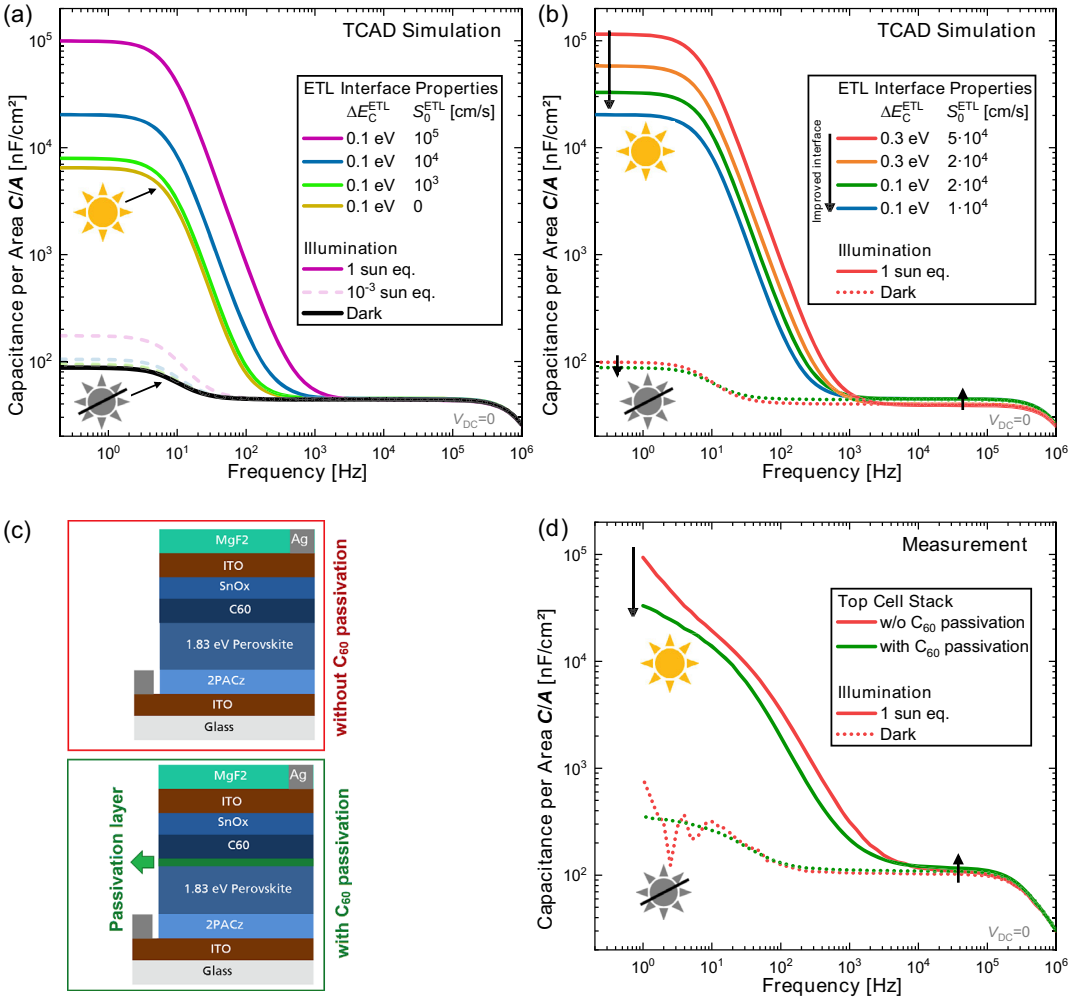

Figure 5. a) Simulated capacitance per area C/A as a function of the AC frequency at a DC voltage $V_{DC} = 0$ V for varied surface recombination velocities at the perovskite/ETL interface (S_0^{ETL}) for both illuminated case (solid lines) and dark case (black line). The transparent dashed lines show the impact of very low illumination. b) Simulated capacitance per area C/A as a function of the AC frequency at a DC voltage $V_{DC} = 0$ V for varied conduction band offset at the perovskite/ETL interface ΔE_C^{ETL} and S_0^{ETL} for both illuminated (solid lines) and dark case (dotted lines). c) Layer stacks of two experimental test structures built at Fraunhofer ISE: the first stack is without passivation of the C_{60}/perovskite interface (shown in red) and the second with C_{60} passivation (green). d) $C(f)$ for the two top cell stacks of (c) measured at IMEC for illuminated case (solid lines) and dark case (dotted lines).

measured for C_{60}/LiF/perovskite layer stacks[22]) and a surface recombination velocity at the interface of $S_0^{ETL} = 10^4$ cm s^{-1} (referring to the minorities, i.e., in this case the holes). (Note that S_0^{ETL} is a quantity for the chemical surface passivation and that the effective surface recombination is influenced by the interplay between the chemical and field-effect passivation. As the field-effect passivation of a C_{60}/LiF/perovskite layer stack is improved,[22] the recombination is suppressed despite a high S_0^{ETL} [15]) It can be seen that the low-frequency plateau is now several orders of magnitude higher with around 2×10^4 nF cm^{-2} (note the logarithmic scale of the y-axis) than it has been for the dark case which is shown as solid dark line (equal to Figure 3b). Figure 5a shows that the low-frequency capacitance of the illuminated perovskite device presents a clear dependency for varied S_0^{ETL} : For a very high S_0^{ETL} of 10^5 cm s^{-1} (purple line), the capacitance under illumination lies at 1×10^5 nF cm^{-2} which is 5 times higher than for the blue case. For lower S_0^{ETL} of 10^3 cm s^{-1} (light green line), the capacitance under illumination lies at about 8×10^3 nF cm^{-2}, while without any recombination at the interface (yellow line) the capacitance slightly drops to about 6×10^3 nF cm^{-2}. All values are significantly higher than the dark case which lies at 90 nF cm^{-2} for all S_0^{ETL} and is therefore independent of the surface recombination at the ETL interface. This is due to the reason that in the dark the asymmetry between electron and hole concentration at the ETL/perovskite interface (n/p) is very high; therefore, surface recombination is negligible as (almost) no holes are available at the interface to recombine. However, the transparent dashed lines in Figure 5a show the impact of a very low illuminated of only 10^{-3} suns equivalent (i.e., "almost dark") which yields a significant difference for the high recombination device (purple dashed line) of about factor 2 compared to the absolute dark case

(in black). This underlines that it is important for "dark" capacitance measurements to ensure complete darkness (by sufficient coverage of the sample) and that only darkening the lab is not sufficient for reliable measurements. For all measurements carried out in this article, we ensured that the experimental conditions for the perovskite were indeed completely dark. Note that this very-low-light dependence is typical to perovskite cells which have a very high absorption coefficient and it would not be seen in, e.g., for silicon technologies to the same extent.

Figure 5b shows the impact of varied conduction band offset at the ETL/perovskite interface ΔE_C^{ETL}. Starting with the case of the blue solid line (which is equal to the blue solid line of Figure 5a), we first change the surface recombination S_0^{ETL} from $1 \times 10^4\,cm\,s^{-1}$ (blue solid line) to $2 \times 10^4\,cm\,s^{-1}$ (green solid line) which increases the low-frequency capacitance of the illuminated sample, while the capacitance of the sample in the dark is unchanged (i.e., the dotted blue and dotted green lines match exactly). This is in line with what was discussed in Figure 5a. When the conduction band offset at the ETL/perovskite interface ΔE_C^{ETL} is changed from 0.1 eV (green) to 0.3 eV (orange), the TCAD simulation of the illuminated perovskite device predicts a low-frequency capacitance plateau that is further increased, while the high-frequency plateau (around 10^4 Hz) is decreased. When further increasing the surface recombination S_0^{ETL} from $2 \times 10^4\,cm\,s^{-1}$ (solid orange line) to $5 \times 10^4\,cm\,s^{-1}$ (red solid line), again only the low-frequency capacitance of the illuminated sample is increased, while the capacitance of the sample in the dark is unchanged (i.e., again, the dotted orange and dotted red line match exactly). Most interestingly, while the surface recombination S_0^{ETL} does not change the capacitance response of the dark case, it is influenced by the change in band offset ΔE_C^{ETL} (red dotted vs green dotted line). This is due to the reason that a decreasing ETL/perovskite band offset increases the built-in potential of the device, thus the electric field within the perovskite absorber, which hampers the displacement of anions away from the interface according to Section 3.3. This leads to a lower capacitance response for low-frequency AC signals. For high frequencies the capacitance response increases with better band alignment, as the quasi-Fermi levels are closer to the band edges leading to higher charge-carrier concentrations, which, when modulated by an AC signal, are reflected in a higher capacitance response. Consequently, the changes in band alignment and recombination velocities could be differentiated principally by analyzing the respective changes in capacitance response for both dark and illuminated cases (as indicated by the black arrows). Practically, this might be difficult as the capacitance under illumination also depends on the HTL properties and bulk recombination properties (not shown).

3.4.2. Experimental Evidence

Experimental test structures were fabricated at Fraunhofer ISE and measured at IMEC to compare to the TCAD simulation model. Figure 5c shows the layer stack of the two samples. The first sample ("without C_{60} passivation," framed in red) is a 0.25 cm^2-sized perovskite single-junction device, featuring an ITO-coated glass substrate, a 1 nm thick 2PACz layer (i.e., a self-assembled monolayer) acting as HTL, a 300 nm thick triple-halide perovskite layer with a bandgap of 1.83 eV ($FA_{0.78}Cs_{0.22}Pb(Br_{0.3}I_{0.7})_3 + 10\%MAPbCl_3$), a 15 nm thick C_{60} layer acting as ETL, a 20 nm thick tin-oxide SnO_x capping layer followed by a 25 nm top ITO for lateral conductance, 200 nm silver (Ag) front contact, and an MgF_2 layer acting as antireflection coating. The second structure is processed identically with the only difference of adding an ultrathin spin-coated passivation layer of piperazinium iodide (highlighted in green) to the C_{60}/perovskite interface, from which better device performance is expected, either due to better chemical passivation at the interface or better band alignment (i.e., field-effect passivation), or both.

Figure 5d shows the measured capacitance per area as a function of the AC frequency around a DC bias voltage of 0 V for both the nonpassivated (shown in red) and the passivated sample (shown in green). The dotted lines show the dark case. One can see a high-frequency plateau around 4×10^4 Hz of about $C/A = 100\,nF\,cm^{-2}$, which is significantly higher than for the perovskite device regarded in Section 3.2 due to the lower perovskite thickness and probably higher dielectric permittivity of the triple-halide perovskite composition. This plateau drops toward very high frequencies, from which the combined series resistance of the device could be adapted by the TCAD simulation model (similar as for the inset of Figure 3b, not shown here) to a value around $R_S = 2.5\,\Omega\,cm^2$. We see that the nonpassivated (red dotted line) and passivated (green dotted line) are mostly equal (despite some measurement artifacts for the nonpassivated sample at low frequencies). However, one could argue to see a slight trend toward an upshift at the high-frequency plateau and a downshift of the low-frequency plateau for the passivated sample with respect to the nonpassivated sample, which could be a hint for a slightly improved band alignment ΔE_C^{ETL} since a change in S_0^{ETL} would not be expected to change the capacitance response of the dark case as discussed in Section 3.4.1. However, as the respective differences are quite low and therefore within the uncertainty of the capacitance measurement technique, this should be subject to future investigations.

Looking at the measured capacitance response of Figure 5d for the case with 1 sun equivalent illumination, we see that for frequencies below 10^4 Hz, the capacitance drastically increases by around three orders of magnitude which is consistent with the expected trend from the TCAD simulation of Figure 5b. Most interestingly, the capacitance for the nonpassivated sample under illumination (solid red line) lies around $1 \times 10^5\,nF\,cm^{-2}$ for $f = 1$ Hz, while the capacitance for the passivated sample under illumination (solid green line) is significantly lower and lies only at $\approx 3 \times 10^4\,nF\,cm^{-2}$. Furthermore, for the 10–100 kHz regime, the capacitance for the passivated sample is slightly higher. Both trends are indicated by the black arrows and correspond to the trend that was seen in the TCAD modeling of Figure 5b when the conduction band alignment at the ETL interface ΔE_C^{ETL} and surface recombination S_0^{ETL} was improved (from red to green case).

To sum up, when comparing Figure 5b,d, we obtained a very good agreement of the TCAD model with measured experimental test structures for both the dark and illuminated case and discussed two key parameters of the altered ETL/perovskite interface and their impact on the capacitance response for the dark and illuminated case.

4. Conclusion

In this study, we investigated the role of mobile ions in PSCs and their influence on device performance, particularly through a combined analysis of experiments and simulation of both capacitance-based characterization methods and current–voltage (J–V) characteristics. Within the scope of this work, the optoelectrical simulation model of Sentaurus TCAD was extended to model frequency-dependent capacitance (C–f) characteristics. Our research primarily focused on single-junction solar cells applied in tandem structures with varying bandgaps, but the modeling approach is applicable to a wide range of perovskite-based devices.

The findings of this study underscore the complexity of interpreting capacitance-based measurements in the context of PSCs, particularly when considering the contributions of mobile ions together with the role of transport layers. The TCAD model was compared to equivalent circuit modeling highlighting the importance of considering the depth-dependent inhomogeneities in resistivity, especially in devices with intrinsic transport layers.

The TCAD simulation results were compared and validated against experimental data, showing strong agreement in the capacitance–frequency (C–f) behavior and current–voltage (J–V) characteristics. The correlation between ion migration and scan-time-dependent J–V hysteresis was demonstrated, linking specific ion properties to observable device behavior. This validation confirms the effectiveness of our model in accurately capturing the dynamics of mobile ions within PSCs. An in-depth analysis of the simulated devices reveals how the capacitance is increased for frequencies below the characteristic frequency of the ion species due to the displacement of mobile ions facilitating additional charge-carrier accumulation in the device.

In a last section, we elaborated on the C–f characteristics of PSCs under illumination. By means of the TCAD simulation, we could show the impact of the surface recombination velocity and band alignment at the perovskite/ETL interface for both dark and illuminated cases. Experimental PSC test structures that were fabricated with and without ETL passivation at Fraunhofer ISE and measured at IMEC, revealing a very good agreement with the simulation model, and revealing that the expected reduction of interface recombination due to the ETL passivation indeed leads to the expected reduction in capacitance response for low frequencies. The dark characteristics indicated that the surface modifications due to the ETL passivation layer are not only linked to a reduced surface recombination velocity, but probably also linked to an improved band alignment at the ETL/perovskite interface.

In conclusion, our work enhances the understanding of the mobile ion dynamics in PSCs and the relation to capacitance-based methods for evaluating device parameters. Future work should focus on further refining the simulation model to incorporate additional physical phenomena like different DC voltages and expanding the experimental validation across a wider range of perovskite compositions and device architectures.

Supporting Information

Supporting Information is available from the Wiley Online Library or from the author.

Acknowledgements

This work was partially supported by the European Union through the Horizon Europe project Triumph under the number 101075725 and the German Federal Ministry for Economic Affairs and Climate Action (BMWK) under contract number 03EE1132A (RIESEN). The authors would like to thank Athira Shaji for processing of the solar cells at ISE.

Conflict of Interest

The authors declare no conflict of interest.

Author Contributions

Christoph Messmer: Conceptualization (lead); Data curation (lead); Formal analysis (lead); Investigation (lead); Methodology (lead); Software (lead); Validation (lead); Visualization (lead); Writing—original draft (lead); Writing—review and editing (lead). **Jonathan Parion**: Investigation (supporting); Methodology (supporting); Validation (supporting); Writing—review and editing (supporting). **Cristian V. Meza**: Investigation (supporting); Validation (supporting). **Santhosh Ramesh**: Investigation (supporting). **Martin Bivour**: Conceptualization (supporting). **Minasadat Heydarian**: Investigation (supporting); Writing—review and editing (supporting). **Jonas Schön**: Conceptualization (supporting); Formal analysis (supporting); Funding acquisition (lead); Project administration (lead); Supervision (lead); Validation (supporting); Visualization (supporting); Writing—review and editing (supporting). **Hariharsudan S. Radhakrishnan**: Conceptualization (supporting); Funding acquisition (supporting); Project administration (supporting); Supervision (supporting). **Martin C. Schubert**: Funding acquisition (supporting); Project administration (supporting); Supervision (supporting). **Stefan W. Glunz**: Funding acquisition (supporting); Project administration (supporting); Supervision (supporting); Writing—review and editing (supporting).

Data Availability Statement

Research data are not shared.

Keywords

characterization, perovskite solar cells, simulations

Received: August 29, 2024
Revised: October 24, 2024
Published online: November 19, 2024

[1] H. J. Snaith, A. Abate, J. M. Ball, G. E. Eperon, T. Leijtens, N. K. Noel, S. D. Stranks, J. T.-W. Wang, K. Wojciechowski, W. Zhang, *J. Phys. Chem. Lett.* **2014**, *5*, 1511.
[2] V. M. Le Corre, J. Diekmann, F. Peña-Camargo, J. Thiesbrummel, N. Tokmoldin, E. Gutierrez-Partida, K. P. Peters, L. Perdigón-Toro, M. H. Futscher, F. Lang, J. Warby, H. J. Snaith, D. Neher, M. Stolterfoht, *Sol. RRL* **2022**, *6*, 2100772.
[3] P. Calado, A. M. Telford, D. Bryant, X. Li, J. Nelson, B. C. O'Regan, P. R. F. Barnes, *Nat. Commun.* **2016**, *7*, 13831.
[4] M. V. Khenkin, E. A. Katz, A. Abate, G. Bardizza, J. J. Berry, C. Brabec, F. Brunetti, V. Bulović, Q. Burlingame, A. Di Carlo, R. Cheacharoen, Y.-B. Cheng, A. Colsmann, S. Cros, K. Domanski, M. Dusza, C. J. Fell, S. R. Forrest, Y. Galagan, D. Di Girolamo, M. Grätzel, A. Hagfeldt, E. von Hauff, H. Hoppe, J. Kettle, H. Köbler, M. S. Leite, S. Liu, Y.-L. Loo, J. M. Luther, et al., *Nat. Energy* **2020**, *5*, 35.

[5] C. Messmer, D. Chojniak, A. J. Bett, S. K. Reichmuth, J. Hohl-Ebinger, M. Bivour, M. Hermle, J. Schön, M. C. Schubert, S. W. Glunz, *Prog. Photovoltaics: Res. Appl.* **2024**.
[6] J. Herterich, M. Unmüssig, G. Loukeris, M. Kohlstädt, U. Würfel, *Energy Technol.* **2021**, *9*, 2001104.
[7] M. T. Neukom, A. Schiller, S. Züfle, E. Knapp, J. Ávila, D. Pérez-Del-Rey, C. Dreessen, K. P. S. Zanoni, M. Sessolo, H. J. Bolink, B. Ruhstaller, *ACS Appl. Mater. Interfaces* **2019**, *11*, 23320.
[8] F. Recart, A. Cuevas, *IEEE Trans. Electron Devices* **2006**, *53*, 442.
[9] M. Taukeer Khan, F. Khan, A. Al-Ahmed, S. Ahmad, F. Al-Sulaiman, *Chem. Rec.* **2022**, *22*, e202100330.
[10] S. Ravishankar, Z. Liu, U. Rau, T. Kirchartz, *PRX Energy* **2022**, *1*, 013003.
[11] M. C. Schmidt, E. Gutierrez-Partida, M. Stolterfoht, B. Ehrler, *PRX Energy* **2023**, *2*, 043011.
[12] Synopsis, Sentaurus TCAD: Release U-2022.12-SP1 **2023**.
[13] L. Restat, C. Messmer, M. Heydarian, M. Heydarian, J. Schoen, M. C. Schubert, S. W. Glunz, *Sol. RRL* **2024**, *8*, 2300887.
[14] S. Ravishankar, T. Unold, T. Kirchartz, *Science* **2021**, *371*, eabd8014.
[15] J. Liu, M. de Bastiani, E. Aydin, G. T. Harrison, Y. Gao, R. R. Pradhan, M. K. Eswaran, M. Mandal, W. Yan, A. Seitkhan, M. Babics, A. S. Subbiah, E. Ugur, F. Xu, L. Xu, M. Wang, A. U. Rehman, A. Razzaq, J. Kang, R. Azmi, A. A. Said, F. H. Isikgor, T. G. Allen, D. Andrienko, U. Schwingenschlögl, F. Laquai, S. de Wolf, *Science* **2022**, *377*, 302.
[16] J. Parion, S. Ramesh, S. Subramaniam, H. Vrielinck, F. Duerinckx, H. S. Radhakrishnan, J. Poortmans, J. Lauwaert, B. Vermang, *Sol. RRL* **2024**, *8*, 2400529.
[17] V. M. Le Corre, M. Stolterfoht, L. Perdigón Toro, M. Feuerstein, C. Wolff, L. Gil-Escrig, H. J. Bolink, D. Neher, L. J. A. Koster, *ACS Appl. Energy Mater.* **2019**, *2*, 6280.
[18] M. Stolterfoht, C. M. Wolff, Y. Amir, A. Paulke, L. Perdigón-Toro, P. Caprioglio, D. Neher, *Energy Environ. Sci.* **2017**, *10*, 1530.
[19] S. Ravishankar, Z. Liu, Y. Wang, T. Kirchartz, U. Rau, *PRX Energy* **2023**, *2*, 033006.
[20] D. R. Ceratti, A. Zohar, R. Kozlov, H. Dong, G. Uraltsev, O. Girshevitz, I. Pinkas, L. Avram, G. Hodes, D. Cahen, *Adv. Mater.* **2020**, *32*, e2002467.
[21] J. Diekmann, F. Peña-Camargo, N. Tokmoldin, J. Thiesbrummel, J. Warby, E. Gutierrez-Partida, S. Shah, D. Neher, M. Stolterfoht, *J. Phys. Chem. Lett.* **2023**, *14*, 4200.
[22] D. Menzel, A. Al-Ashouri, A. Tejada, I. Levine, J. A. Guerra, B. Rech, S. Albrecht, L. Korte, *Adv. Energy Mater.* **2022**, *12*, 2201109.